# Photoswitchable Liquid Crystal Elastomer Adhesives Operating at Room Temperature

Yudian Wu<sup>a</sup>, Brandon D. Clarke<sup>b</sup>, Kenneth M. Liechti, <sup>b,\*</sup> and Zachariah A. Page<sup>a,\*</sup>

<sup>a</sup>Department of Chemistry, The University of Texas at Austin, Austin, TX 78712, USA

\*Corresponding Authors: zpage@utexas.edu, kml@mail.utexas.edu

**ABSTRACT.** The ability to toggle adhesion between two surfaces on demand using reusable "smart" plastics would enable a myriad of applications where two components require temporary bonding, such as in dry transfer of materials for electronics applications. To this end, light is an attractive stimulus owing to its modularity, low energy consumption, and spatiotemporal control. However, a lack of materials capable of reversible light-triggered adhesion at room temperature exists. Herein, a systematic examination of azobenzene-containing liquid crystal elastomers (LCEs) revealed design principles that relate processing and composition to the performance of photoswitchable adhesives. This led to LCEs capable of reversibly picking up and releasing objects through a simple "flip of the switch" on UV and blue LEDs. Moreover, detailed optical and thermomechanical characterization outlined the modular scope of the present platform and provided insight into the governing mechanism(s) for photoswitchable adhesion, which will serve to inform further optimization. Such stimuli responsive materials have the potential to advance applications in electronics and soft robotics that can benefit from programmable and dynamic adhesion.

#### INTRODUCTION

Materials capable of sensing and responding to environmental stimuli are often referred to as "smart", and they have led to advanced functionality in several applications, including adhesives, soft robotics, sensors, and drug delivery. He within the realm of smart adhesives, pressure, heat, and light have served as common stimuli to facilitate bonding and/or debonding. Light is particularly attractive given its ease of application and potential to provide spatiotemporal control over the adhesive response. However, the predominant light-responsive adhesives are photocurable glues (thermosets), which often suffer from irreversible bonding and residue transfer (contamination) upon removal. Alternatively, linear polymers (thermoplastics) comprising azobenzenes have been placed in the "spotlight" for use as photoswitchable adhesives given their considerable changes in bulk physical properties that occur upon light-triggered E/Z isomerization. Early reports in this area focused on photoisomerization-induced solid-to-liquid transitions of such materials, which arises from decreasing intermolecular interactions (e.g.,  $\pi$ - $\pi$  stacking) in going from E (rod-shaped) to E (bent) azobenzene isomers. However, adhesion tests of these polymers results in cohesive failure, leaving behind residue and preventing repeated use of the adhesive.

Liquid crystal elastomers (LCEs) represent a nascent class of materials for use as smart adhesives. <sup>19</sup> For example, LCEs exhibit characteristics of pressure-sensitive adhesives (PSAs)<sup>20–23</sup> that are compatible with a wide range of substrates and provide residue-free removal. Through modulating the nematic-to-isotropic transition temperature  $(T_{NI})^{19}$  or liquid crystal (mesogen) alignment, <sup>24</sup> adhesive properties (e.g., strength,  $\sigma_{ad}$ ) of LCEs can be tailored (**Figure 1A**). Pioneering work by Ohzono, Terentjev, and coworkers examined thermally-controlled LCE adhesives, <sup>19</sup> followed by photo-controlled azobenzene-containing LCE adhesives. <sup>25,26</sup> Upon exposure to heat or UV light, these LCEs underwent a mesophase change (disordering) that was accompanied by a decrease in adhesion. However, unlike the smart thermoplastics previously mentioned, the unified molecular-level connectivity in these LCEs led to an adhesive over cohesive failure mode. <sup>14</sup> As such, removal of the stimulus followed by thermal annealing to erase history enabled reuse of the adhesives. Notably, for the photoresponsive case, both light and heat along with high pull-of rates ( $\nu \ge 50$  mm/min) were necessary to achieve reversible and significant changes in adhesive strength ( $\Delta \sigma_{ad} \approx 2 \times$ ), providing opportunities for improvement. <sup>26</sup>

<sup>&</sup>lt;sup>b</sup>Department of Aerospace Engineering and Engineering Mechanics, The University of Texas at Austin, Austin, TX 78712, USA

The leading rationales for the observed stimuli-responsive change in adhesion within LCEs are perturbations in energy dissipation mechanisms and surface-to-surface contact area (**Figure 1B**).  $^{20,21}$  The purported energy dissipation mechanisms in LCEs are soft elasticity, caused by macroscopic reorientation of the nematic director (i.e., mesogen orientation) upon deformation,  $^{27-30}$  and/or high-frequency microscopic rotations of the nematic director. In both mechanisms, the density of intermolecular interactions between mesogens (e.g.,  $\pi$ - $\pi$  stacking) is paramount. However, reducing the glass transition temperature ( $T_g$ ) and  $T_{NI}$  to increase contact area under ambient conditions has primarily been accomplished by diluting the mesogen with flexible, non-liquid crystalline spacers such as tripropylene glycol diacrylate (TPGDA) (**Figure 1C**).  $^{32-34}$  As such, within LCE adhesives a contemporary tradeoff exists between energy dissipation (~high [LC]) and conformal contact at room temperature (~low [LC]).

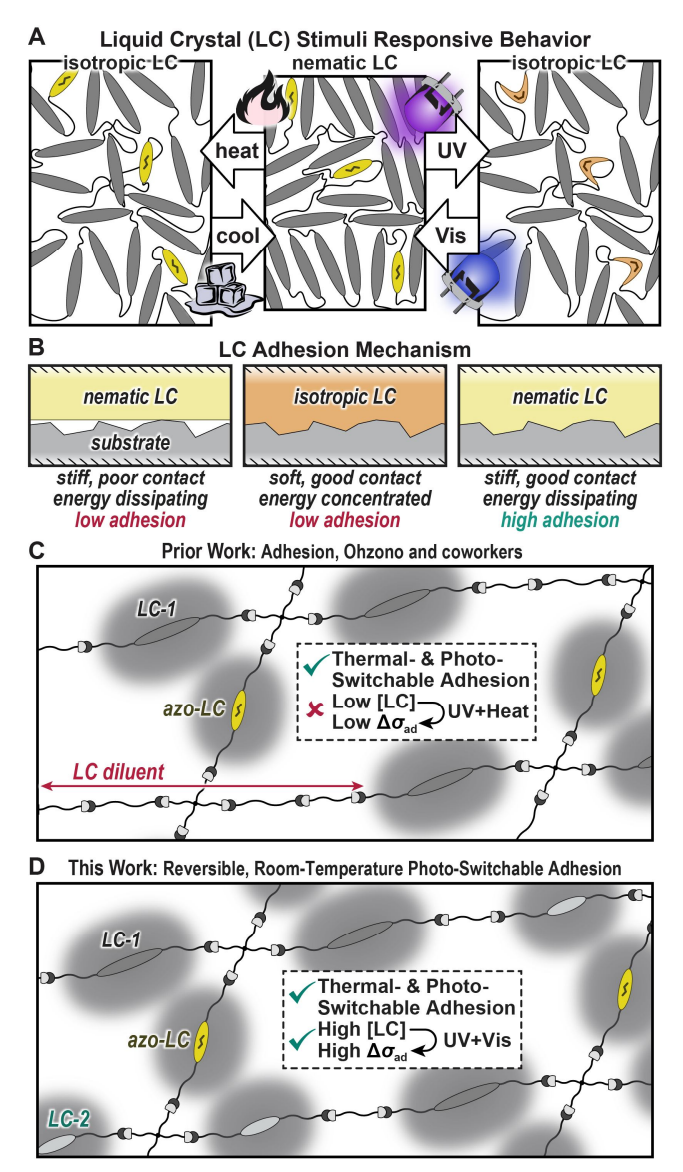


**Figure 1.** Illustrations of photoresponsive liquid crystal elastomer (LCE) adhesives. (A) Order-to-disorder transitions going between isotropic and polydomain nematic mesophases upon changing temperature or illumination conditions (UV  $\nu s$ . visible). (B) LC adhesion mechanisms between a smooth and rough surface. (C/D) LCE networks from prior/present work with relative length of LC and chain extender (i.e., diluent) components ~to scale, where an increase in LC concentration ([LC]) in this work enhances the change in adhesion strength ( $\Delta \sigma_{ad}$ ) upon UV and visible light exposure at room temperature.

Herein, a novel LCE formulation that overcomes this tradeoff is revealed. A second LC monomer is incorporated in place of more traditional non-LC spacers while maintaining low  $T_g$  and  $T_{NI}$  values for room temperature photoswitchable adhesion (**Figure 1D**). Furthermore, a systematic examination of LCE processing parameters, composition, photoisomerization kinetics, and corresponding mesophase changes provided key design principles for reversible light-driven bonding and debonding at room temperature. Overall, the present formulation provides significant changes in adhesion ( $\Delta \sigma_{ad} \approx 2 \times$ ) at modest pull-off rates (0.6 mm/min) using only two distinct wavelengths of light under ambient conditions, while maintaining reproducible performance over several cycles.

### **RESULTS & DISCUSSION**

### 3. 1. LCE Matrix Design

The photoswitchable LCE adhesives were prepared from commercial reactive mesogens and chain extenders capable of undergoing an efficient thiol-Michael addition polymerization upon addition of a base catalyst (**Figure 2**). Specifically, 1,4-bis[4-(6-acryloyloxyhexyloxy)benzoyloxy]-2-methylbenzene (C6M) served as the predominant LC monomer, while 4,4'-bis(6-acryloyloxyhexyloxy)azobenzene (AZO), synthesized in-house (see SI for details), served as the photoresponsive unit. Non-LC thiol and acrylate chain-extenders 2,2'-(ethylenedioxy)diethanethiol (EDDET) and tripropylene glycol diacrylate (TPGDA) as a control, respectively, were used in conjunction with pentaerythritol tetrakis(3-mercaptopropionate) (PETMP) as the crosslinker. Note that the concentrations for EDDET (39.5 mol%) and PETMP (7 mol%) were held constant throughout (see Table S1 in the SI for a comprehensive list of compositions). To lower  $T_{NI}$  without considerably altering  $T_g$  we examined the influence of exchanging non-LC TPGDA with LC 4-(6-(acryloyloxy)hexyloxy)phenyl 4-(6-(acryloyloxy)hexyloxy)benzoate (C6BAPE). This decision was inspired by recent reports showing that the two phenyl rings of C6BAPE led to weaker  $\pi$ - $\pi$  interactions relative to C6M having three phenyl rings,  $^{35}$  while also forming a eutectic phase when mixed with C6M, both causing a decrease in  $T_{NI}$ . One hypothesis was that replacing TPGDA with C6BAPE would increase the density of intermolecular interactions in the polydomain nematic mesophase, and in turn increase the

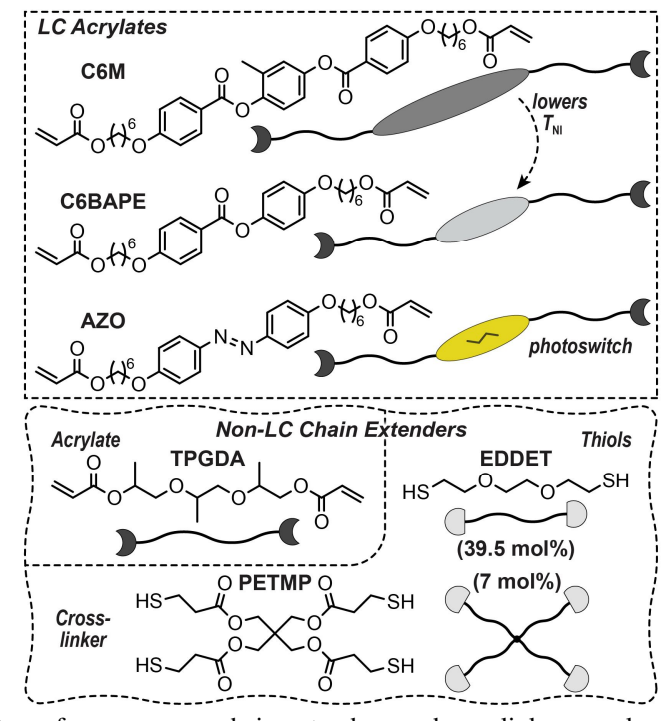


Figure 2. Chemical structures for monomers, chain-extenders, and crosslinkers employed in this study.

adhesion energy of the LCE. Simultaneously, the enhanced "communication" within the LCE matrix containing a higher [LC] was hypothesized to result in a more pronounced response (e.g., larger shift in the  $T_{\rm NI}$ ) upon exposure to light under equivalent conditions.

# 3.2. LCE Processing Conditions

The LCEs were cast neat (without solvent) by melting the monomer mixture at ~100 °C, adding dipropylamine (DPA, 1.5 wt%), and then injecting the homogenous solution between clean glass slides with a gap of ~30  $\mu$ m (**Figure 3A**). Subsequently, curing was accomplished at a specified temperature (described below) for ~14 hours, followed by washing with acetone to remove any residual unreacted material. This bulk casting method avoids the use of commonly employed toxic solvents, such as toluene, and mitigates void formation upon solvent evaporation, thereby facilitating the formation of uniform LCE films for adhesive testing. However, one issue that arose with solvent-free casting was phase separation between the LC and non-LC components, an issue that has previously been observed for analogous LCE processing. <sup>37,38</sup>

To determine an optimal curing temperature, we employed a polarized optical microscope (POM) in a standard trans-illumination configuration to monitor phase separation of the monomer mixtures along with mesophase changes of the resultant LCEs during temperature ramps (**Figure 3B/C**). Samples were placed on a temperature-controlled stage between two perpendicular (crossed) polarizers, and a red LED centered at 625 nm was employed for transmission measurements to avoid activation of AZO (Figures S1-S2). At room temperature all samples adopted a polydomain nematic mesophase (Figure S3), which were birefringent and thus rotated light. On the POM this resulted in transmission of the red light to the camera, while heating the samples above  $T_{\rm NI}$  resulted in an isotropic phase with no light transmission (i.e., no rotation of light), making the samples appear dark.<sup>39</sup> The dramatic change in red light transmission (i.e., intensity,  $I^*$ ) measured by the camera indicated a change in molecular level ordering. In fact, using Haller's approximation, the scalar order parameter (S) is linearly proportional to  $\sin^{-1}(\sqrt{I^*})$ .<sup>40-42</sup> Consequently, for the present samples  $T_{\rm NI}$  was defined as the inflection point of the normalized intensity vs. temperature curves (see *section S3.1* of the SI for more details).

Initially, monomer mixtures containing TPGDA (15.6 mol% to bulk), AZO (9.1 mol% to bulk, 25 mol% relative to LC monomers only), and C6M (27.3 mol% to bulk) were tested upon cooling from 60 to 15 °C at a rate of 3 °C/min (Figure 3B, gray lines). At 50 °C LC monomers began to phase separate from the chain-extenders, forming microcrystals suspended in an isotropic matrix, which was accompanied by a slight increase in red light intensity (Figure 3B, top images). Cooling to 30 °C led to a sharp increase in transmitted light, corresponding with the nucleation and growth of larger phase-separated crystalline domains until 20 °C. Differential scanning calorimetry (DSC) of the monomer mixture showed a small transition attributed to T<sub>NI</sub> at 30 °C (Figure S3). To examine the influence of phase separation on LCE properties, samples were melted between glass slides and cured at 70  $^{\circ}$ C (no phase separation, above  $T_{\rm NI}$ ), 25 °C (large phase separation, below  $T_{\rm NI}$ ), and 40 °C (small phase separation, near  $T_{\rm NI}$ ) (Figures S4-6). LCEs cured at 70 °C were qualitatively transparent (Figure S4) and between crossed polarizers were dark at all temperatures above 10 °C. This likely arose from locking the LCE mixture in a disordered state during crosslinking (i.e., isotropic genesis). In contrast, curing LCEs at 25 °C resulted in qualitatively opaque samples that were birefringent across a broad range of temperatures (from 10 to ≥100 °C). The broad transition (Figure S5) was attributed to the formation of mixed LCE phases that arose from phase separation, leading to crystalline domains surrounded by what was presumed to be a polydomain nematic matrix. Finally, curing at 40 °C provided LCEs with a desired sharp bright-to-dark transition at ~50 °C upon heating (and cooling, Figure S7), indicative of a clean  $T_{\rm NI}$  that likely arises from nematic genesis prior to considerable phase separation (Figure 3B, black lines and inset images). This general procedure was followed to determine optimal processing parameters (i.e., curing conditions) for all subsequent LCE compositions (Table S1).

The curing conditions for monomer mixtures containing C6BAPE in place of TPGDA were optimized next (**Figure 3C**). Specifically, the monomer mixture contained C6BAPE (19.5 mol% to bulk), AZO (13 mol% to bulk, 25 mol% relative to LC monomers only), and C6M (19.5 mol% to bulk). Note that the [AZO] relative to LC monomers only was held constant (25 mol%), which was used as the rationale in designing this composition. However, for clarity in the discussion, only values relative to bulk will be referenced going forward (see Table S1 in the SI for a comprehensive list of compositions). Cooling the monomer mixture from 60 to 15 °C at a rate of 3 °C/min on the POM revealed a clean (i.e., no phase separation) dark-to-bright transition at 20 °C, which was attributed to  $T_{NI}$  (**Figure 3C**, gray lines, and Figure S3). Based on this result, curing at 40 °C provided an LCE with a  $T_{NI}$  of 50 °C, as seen on the POM (**Figure 3C**, black lines and inset images). Due to the lack of apparent phase separation, LCEs comprising C6BAPE could be

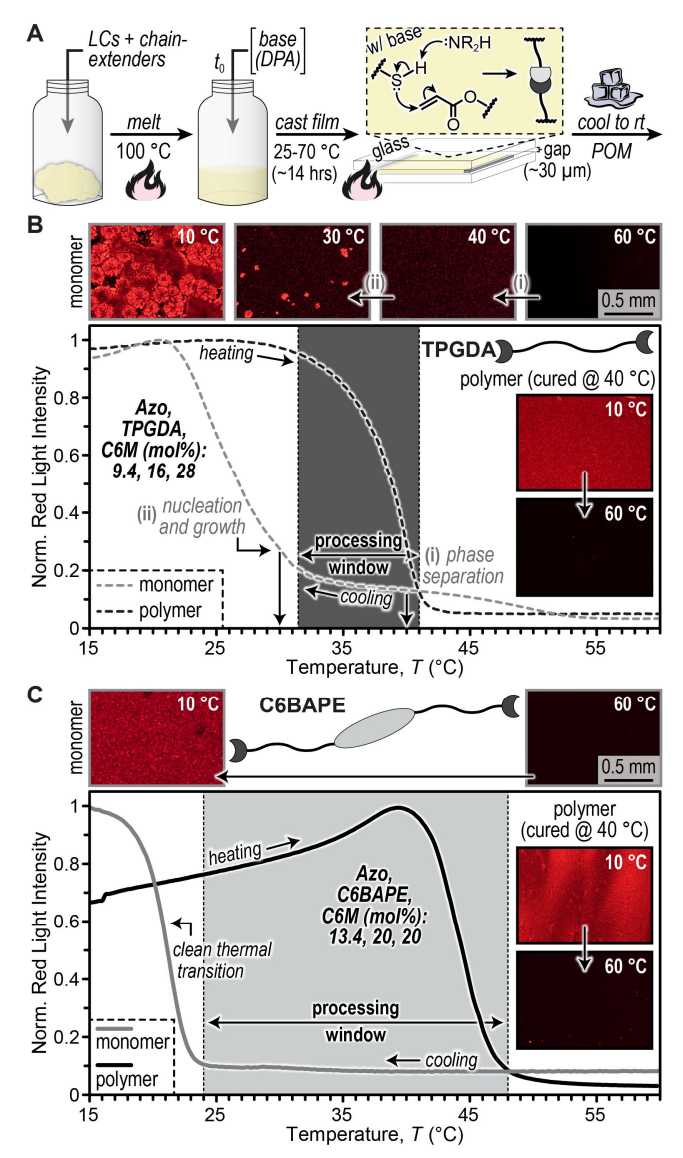


**Figure 3**. General optimization process in preparing LCEs. (A) Illustration showing the process to prepare thin films for monomer mixture testing (without dipropylamine, DPA) or to prepare LCEs (with DPA) for characterization with a polarized optical microscope (POM). Sample illumination with red light was used on the POM to avoid AZO absorption. (B) Representative monomer mixture and corresponding LCE containing TPGDA upon cooling and heating in the POM, respectively. Images of monomer mixture (top) and LCE (inset). (C) Representative monomer mixture and corresponding LCE containing C6BAPE (no TPGDA) upon cooling and heating in the POM, respectively. Images of monomer mixture (top) and LCE (inset).

processed across a wide range of temperatures, including room temperature, from ~25-50 °C (**Figure 3C**, light gray shaded region). Curing at any of these temperatures provided samples with qualitatively similar thermal behavior on the POM (Figure S7). This showcased a distinct advantage over samples comprising TPGDA, which had a restricted processing window above room temperature, ~30-40 °C (**Figure 3B**, dark gray shaded region).

#### 3.3. Correlating LCE Composition to $T_{NI}$ Photoresponse

We hypothesized that UV light exposure that induces E-to-Z isomerization of AZO units would cause a decrease in the extent of order and in turn depress the  $T_{\rm NI}$  relative to non-irradiated regions. To monitor the influence of E-to-Z photoisomerization on LCE ordering, we modified the POM setup to enable top-down illumination, while simultaneously controlling temperature and measuring the intensity of transmitted red light (**Figure 4A**). This was accomplished using epi-illumination with a UV LED centered at 365 nm having an intensity of 50 mW/cm<sup>2</sup> at the sample (Figure S2). The epi-illumination path contained first a hexagonal iris that allowed for irradiation to be confined within the field of view, followed by a 520-nm dichroic filter within a filter cube. The trans-illumination path remained the same as previously described, with the addition of a 525-nm longpass filter on the outgoing "emission" port of the filter cube to block UV light (or blue light, described later) from the camera.

Based on our hypothesis, we anticipated that heating birefringent LCEs from room temperature would provide initially red images throughout the field of view, followed by a dark hexagonal region appearing in the center of the image where the sample was being irradiated with UV light, and then the entire image would become dark as the non-irradiated regions crossed  $T_{\rm NI}$  (**Figure 4A**, top right inset). In practice, this is what was observed, as shown with a representative sample comprising AZO (4.5 mol%), TPGDA (8 mol%), and C6M (40.9 mol%) (**Figure 4B** and Figures S8 and Movie S1). The shift in  $T_{\rm NI}$  for irradiated vs.

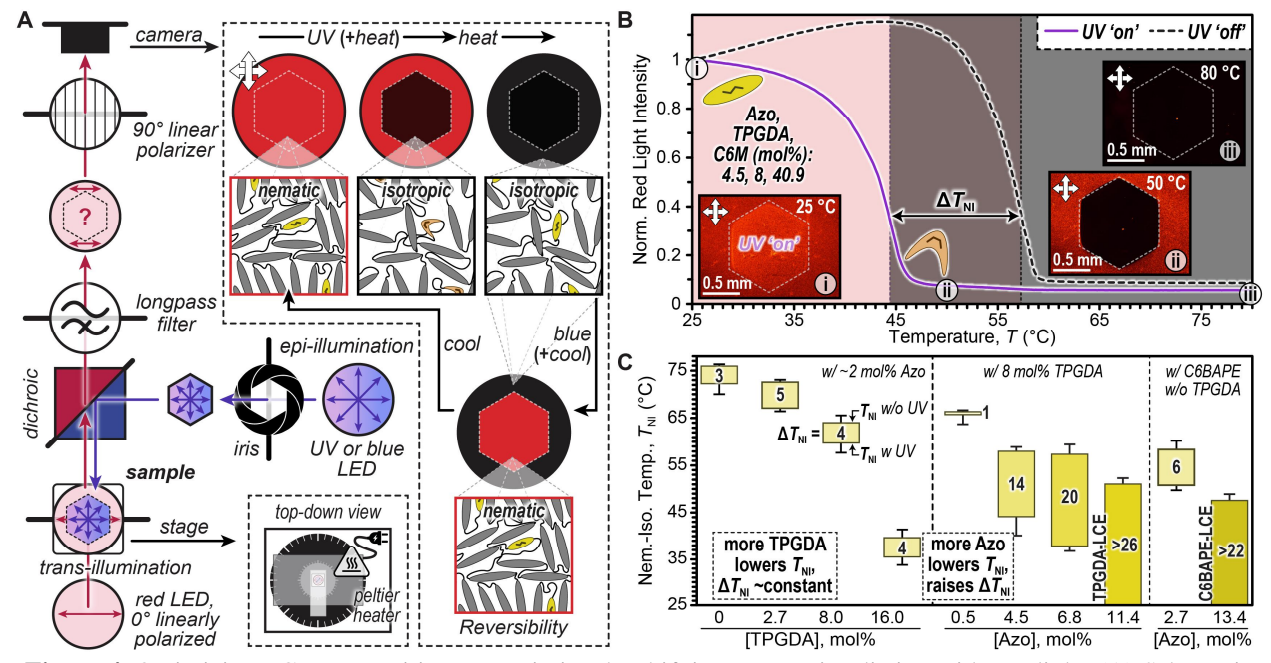


**Figure 4.** Optimizing LCE composition to maximize the shift in  $T_{\rm NI}$  upon irradiation with UV light. (A) Schematic of polarized optical microscope (POM) setup used to monitor changes in birefringence during temperature sweeps with simultaneous trans-illumination (red light) and epi-illumination (UV or blue light). Epi-illumination with UV or blue light was in the shape of a hexagon confined within the field of view. (B) Representative plot of normalized red-light intensity outside (i) and inside (ii) a UV-irradiated hexagon (50 mW/cm²) as a function of temperature used to determine  $T_{\rm NI}$  and  $\Delta T_{\rm NI}$ . Sample was heated from 25 to 80 °C at a rate of 3 °C/minute. (C) Summary of  $T_{\rm NI}$  and  $\Delta T_{\rm NI}$  values for LCEs of varying TPGDA, AZO, C6M, and C6BAPE composition.

non-irradiated regions provided a metric ( $\Delta T_{\rm NI}$ ) to quantify the extent of polydomain disordering that occurred for samples with differing composition. For the representative example (**Figure 4B**),  $\Delta T_{\rm NI} = 14$  °C. However, the UV-irradiated  $T_{\rm NI}$  value in these samples was above room temperature (= 44 ± 1 °C), precluding their utility as photoswitchable adhesives under ambient temperature conditions. Notably, imaging irradiated samples under the present conditions with a thermal camera showed a <1 °C temperature increase, which confirmed that  $\Delta T_{\rm NI}$  values larger than this could be attributed to photoisomerization as opposed to a photothermal effect.

Employing this POM characterization strategy for samples with systematic changes in composition provided fundamental structure-to-photoresponse relationships to ultimately enable UV-irradiated  $T_{\rm NI}$  values below room temperature (~25 °C) (**Figure 4C** and Table S2). Initially varying [TPGDA] at a fixed C6M:AZO of 19, providing [AZO] from 1.9-2.7 mol%, showed only a significant influence on the position of  $T_{\rm NI}$  and not  $\Delta T_{\rm NI}$ , with the shift being 3-5 °C for all samples. Specifically, increasing [TPGDA] from 0 to 16 mol% provided mean  $T_{\rm NI}$  values (non-irradiated,  $\geq$ 3 samples) from 76 to 40 °C with  $\pm$  1-2 °C standard deviation. Thus, changing [TPGDA] at ~2 mol% [AZO] did not provide LCEs with photoswitching of  $T_{\rm NI}$  across room temperature.

Next, we varied [AZO] while holding [TPGDA] constant at 8 mol%. The [AZO] had a significant effect on both the position of  $T_{\rm NI}$  and  $\Delta T_{\rm NI}$ . Specifically, increasing the [AZO] from 0.5 to 11.4 mol% decreased  $T_{\rm NI}$  values (non-irradiated) from 66 to 51 °C with  $\pm$  1-2 °C standard deviation. Importantly, this increase in [AZO] also considerably increased  $\Delta T_{\rm NI}$  from 1 to >26 °C, leading to a  $T_{\rm NI}$  shift across room temperature for an [AZO] of 11.4 mol% (= 25 mol% rel. to LC monomers). For convenience we will refer to this composition (AZO, TPGDA, C6M = 11.4, 8, 34.1 mol%, respectively) as TPGDA-LCE, which was carried forward for further experiments. Finally, replacing TPGDA with C6BAPE enabled the preparation of LCEs having low  $T_{\rm NI}$  values without diluting the total amount of LC material. For example, LCEs with 1:1 C6BAPE:C6M (= 25.4 mol% each) and 2.7 mol% had a  $T_{\rm NI}$  value (non-irradiated) of 58  $\pm$  2 °C, while having a  $\Delta T_{\rm NI}$  of 8 °C. Increasing the [AZO] to 13.4 mol% (= 25 mol% rel. to LC monomers) while maintaining a 1:1 C6BAPE:C6M (= 20 mol% each) provided a  $T_{\rm NI}$  value (non-irradiated) of 47  $\pm$  1 °C. Importantly, it provided a  $\Delta T_{\rm NI}$  >22 °C, which led to a shift across room temperature. For convenience we will refer to this composition (AZO, C6BAPE, C6M = 13.4, 20, 20 mol%, respectively) as C6BAPE-LCE, which was carried forward for further experiments.

## 3.4. Reversibility of Room Temperature Photoswitching

For the present AZO system the Z-isomer is the photostationary state, and thus removal of UV light will trigger a reversion back to the original E-isomer dominated thermodynamic equilibrium. Equilibration of Z to E can be accelerated with the application of heat or visible light at a wavelength absorbed by the  $n\rightarrow\pi^*$  band, which is ~450 nm (blue light) for AZO. To examine the thermal stability of the two optimized LCE compositions (TPGDA and C6BAPE) we employed our custom POM setup by first irradiating a hexagonal region with UV light (365-nm LED, 50 mW/cm²) for ~1 minute at room temperature to reach the photostationary state (**Figure 5** and Figure S10). Immediately following this irradiation, the iris was closed slightly, and the center of the UV-irradiated region was irradiated with blue light (470-nm LED, 50 mW/cm², Figure S2). This created three distinct regions within the field of view: (a) UV-irradiated hexagon, (b) blue-irradiated hexagon within the center of the UV-irradiated hexagon, and (c) outside hexagon not exposed to UV or blue light (**Figure 5A/B**, inset).

Samples containing TPGDA displayed reversibility both with and without blue light (**Figure 5A**). In region (a) the TPGDA-LCE recovered to the original polydomain nematic state in  $\sim 10$  minutes, while in region (b) the application of blue light led to a rapid ( $\sim 30$  second) recovery. Notably, the average red-light transmission within the blue irradiated region was  $\sim 30\%$  larger than region (c), where no UV or blue irradiation took place. This indicated an increase in order (S), which we hypothesized arose from blue light exposure shifting the AZO equilibrium to a higher E-to-Z ratio. Similarly, the C6BAPE-LCE responded to

blue-light irradiation by switching from an isotropic phase (region (a)) to a polydomain nematic mesophase (region (b)) that ultimately had an increased red-light transmission relative to the control region (c) (**Figure 5B**). In contrast to the TPGDA-LCE, the C6BAPE-LCE did not thermally relax in region (a) over the course of the 10-minute experiment at room temperature, indicating that the isotropic form was trapped in a metastable state. Furthermore, the phase transition with blue light exposure was considerably slower for the C6BAPE-LCE, taking ~120 seconds to recover to the original red-light intensity, followed by a slow recovery that appeared to continue past 10 minutes. This distinct behavior is hypothesized to arise from the larger [LC] when using C6BAPE in-place of TPGDA, leading to more intermolecular interactions that slows the molecular reorientation required for (meso)phase transitions. Overall, the room temperature stability of C6BAPE-LCEs relative to TPGDA-LCEs was viewed favorably for applications in photoswitchable adhesion by providing discrete control over each (meso)phase.

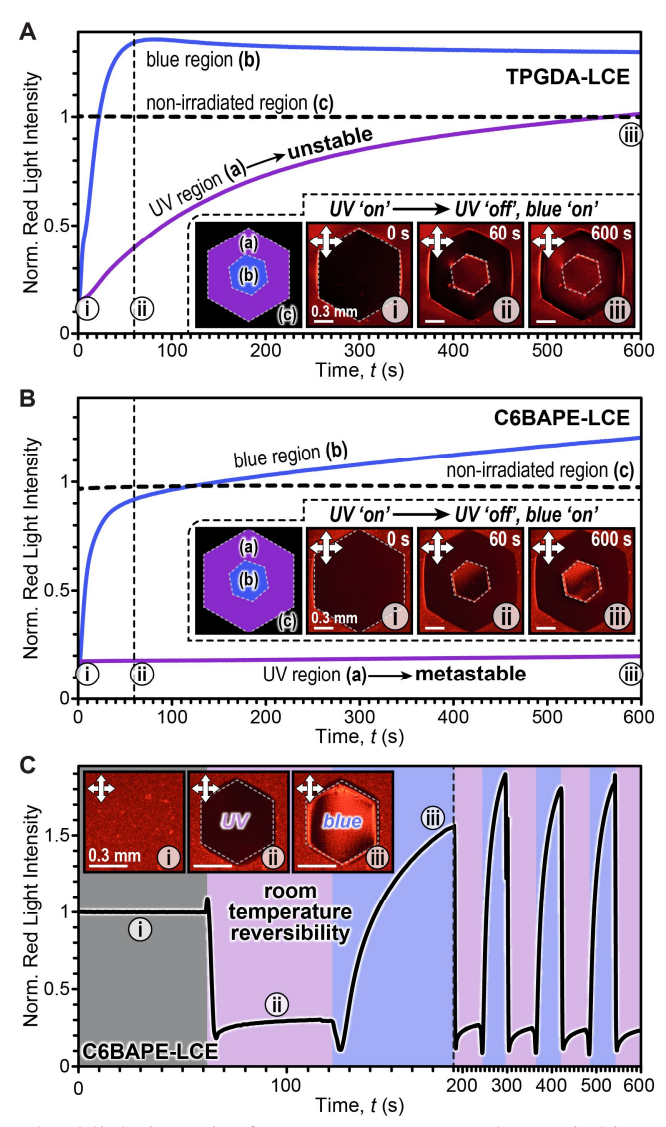


**Figure 5.** Plots of transmitted red-light intensity for room temperature photoswitching of LCE (meso)phases using UV- and blue-light irradiation on the custom POM setup. (A) TPGDA- and (B) C6BAPE-LCEs irradiated first with UV light (365 nm LED, 50 mW/cm², 1 minute) in a hexagon shape (region (a)), followed by irradiation with blue light (470 nm LED, 50 mW/cm²) in a small hexagon (region (b)) within the original UV-irradiated hexagon. Plot shows intensity of these two regions along with the non-irradiated background (region (c)) as a control. (C) Cyclic irradiation of C6BAPE-LCE using UV light (50 mW/cm²) and blue light (50 mW/cm²) in the same iris position for 60 second intervals at room temperature (25 °C).

To assess the repeatability of room temperature (25 °C) photoisomerization, C6BAPE-LCEs were subjected to cyclic UV-blue light irradiation (**Figure 5C**, and Movie S2). In this test the iris position remained static to enable rapid switching between the two light sources, which were connected through a 390-nm dichroic filter cube equipped with a liquid light guide that was coupled to the epi-illumination tube (Figure S1). Irradiating the sample for 60 seconds revealed rapid and reversible photoswitching between isotropic (UV-irradiation) and nematic (blue irradiation) (meso)phases. Notably, the photostationary equilibrium appeared to return to the same position after the first light-cycle, which was attributed to an erasure of the thermal history within the originally prepared sample. This result showcases the potential for C6BAPE-LCEs to be reused for room temperature photoswitchable adhesive applications.

#### 3.5. Photoswitchable Adhesion

A tack test using temperature-controlled (photo)rheology was employed to characterize adhesive properties of the LCEs with a quartz surface (**Figure 6A**). Circular samples with a radius of 6 mm were punched from ~0.5 mm thick LCE films and bonded to a Peltier plate using a thin piece of stiff and strong thermal tape to mitigate adhesive interactions between the LCE and tape influencing measurement results. Subsequently, the samples were pressed onto a quartz plate with top-down heating and/or bottom-up irradiation, followed by removal at a fixed rate while measuring the nominal stress-displacement response. The specific method used for the first set of tack tests was as follows: 1) heat above  $T_{\rm NI}$  (100 °C) to erase thermal history, 2) press LCE onto the quartz plate at a rate of 0.6 mm/minute to a compressive force of 1 N, 3) cool LCE to 20 °C under a constant 1 N force, then heat to the target detachment temperature under a constant 1 N force for 1 minute, and 4) pull the LCE off the quartz plate at a rate of 0.6 mm/min (see *section S2.6* in the SI for more details). This method was used with or without continuous UV light irradiation (365 nm, 50 mW/cm²), and the peak nominal stress (peak tensile force divided by sample area) upon detachment was recorded as the adhesion strength ( $\sigma_{\rm ad}$ ) for each LCE. Although the full stress-displacement curves can provide insight into the debonding mechanism and other adhesion interaction properties, in this study only  $\sigma_{\rm ad}$  is discussed.

Tack tests with C6BAPE-LCE and TPGDA-LCE were conducted with and without UV light exposure and at different detachment temperatures (**Figure 6B**, Figure S11 and Table S3). For C6BAPE-LCEs, detachment at room temperature (25 °C) provided a  $\sigma_{ad}$  of 181 ± 12 kPa, while detachment at 70 °C, which was above  $T_{NI}$  = 47 °C, gave a  $\sigma_{ad}$  of 52 ± 17 kPa ( $\Delta\sigma_{ad}\approx3\times$ ). Additionally,  $\sigma_{ad}$  at room temperature could be increased by ~3× using faster pull-off rates, up to 600 mm/minute (Figure S12). With UV light exposure, the same sample detached at room temperature provided a  $\sigma_{ad}$  of 57 ± 14 kPa, which was comparable to the heated case without UV light. This corroborates the POM findings showing that C6BAPE-LCE samples irradiated with UV light had a  $T_{NI}$  below room temperature (**Figure 4C**). Notably, TPGDA-LCEs detached at room temperature without UV light irradiation provided a  $\sigma_{ad}$  of 115 ± 12 kPa, which was ~1.6× lower than the analogous tack tests with C6BAPE-LCEs. Moreover, detaching TPGDA-LCEs above  $T_{NI}$  (70 °C) without UV light irradiation and at room temperature (25 °C) with UV light irradiation provided  $\sigma_{ad}$  values of 61 ± 6 kPa and 58 ± 10 kPa, comparable to C6BAPE-LCEs. Therefore,  $\Delta\sigma_{ad}$  values at room temperature with  $\nu$ s. without UV light irradiation were ~50% higher for C6BAPE-LCEs relative to TPGDA-LCEs.

To rationalize the observed differences in  $\sigma_{ad}$  between C6BAPE-LCEs and TPGDA-LCEs we characterized hysteresis of samples under uniaxial tension (**Figure 6C**, Figure S13 and Table S4) which has been previously employed as a proxy for adhesive damping<sup>30</sup>. Using dynamic mechanical analysis (DMA) rectangular samples (23 mm × 3 mm × 0.5 mm, length × width × thickness) were loaded to 20% strain and unloaded to zero force uniaxially, and the area between the loading and unloading portions of each stress-strain curve was recorded as the strain energy density (*U*) arising from hysteresis. From this analysis, the C6BAPE-LCE was found to have a value for U (= 830 kPa) that was ~6× larger compared to TPGDA-LCE (= 140 kPa). This difference in U directly correlates with the difference observed for  $\sigma_{ad}$ . Thus, we postulated that the higher density of intermolecular interactions present in the C6BAPE-LCE relative to TPGDA-LCE resulted in greater energy dissipation below  $T_{NI}$ , and in turn increased  $\sigma_{ad}$ . Moreover, those

interactions were "erased" upon crossing  $T_{\text{NI}}$  via heating or UV light irradiation, resulting in comparable  $\sigma_{\text{ad}}$  values (i.e., similarly weak adhesion) under these stimulated conditions.

The reversibility of C6BAPE-LCE adhesion using tack tests with thermal-UV cycling was examined next to assess the potential for reusing these samples (**Figure 6D**). Following the same four-step method on repeat (**Figure 6A**) the sample was shown to exhibit reproducible changes in  $\sigma_{ad}$  over three cycles. In the absence of UV light irradiation samples provided strong adhesion (~200 kPa), while *E*-to-*Z* photoswitching led to a considerable reduction in adhesion strength (to ~60 kPa), providing a consistent  $\Delta \sigma_{ad}$  of ~3×.

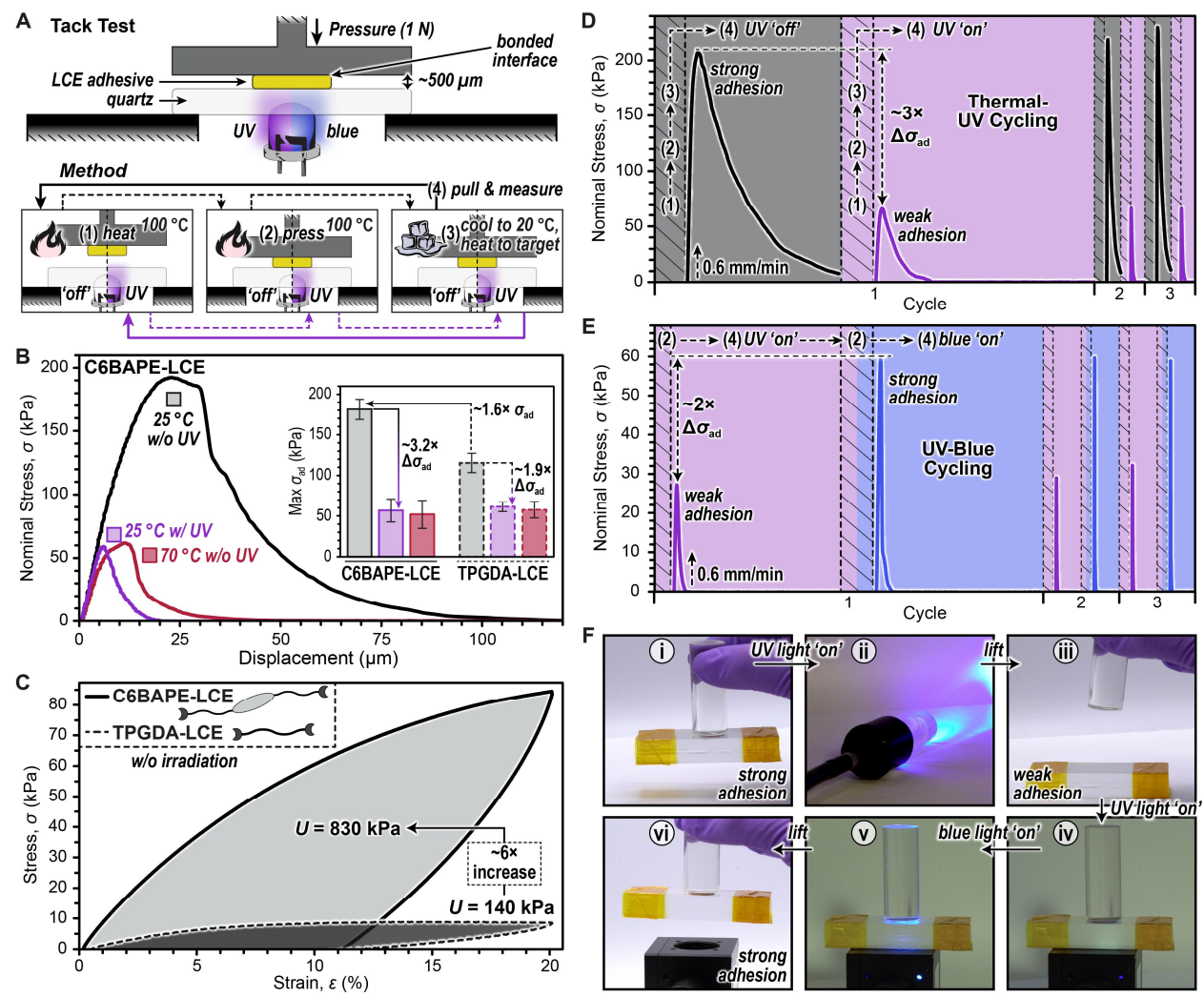


**Figure 6.** Characterizing photoswitchable adhesion using LCEs. (A) Illustration of a tack test using a (photo)rheometer setup to monitor nominal stress as a function of displacement during temperature and light exposure-controlled conditions. The method shows the sequence of steps used for thermal-UV cycling. (B) Representative tack test stress-displacement curves for C6BAPE-LCE at room temperature (25 °C) with and without UV light exposure and above  $T_{\rm NI}$  (70 °C). Inset bar graph shows the mean ( $n \ge 3$ ) adhesion strength ( $\sigma_{\rm ad}$ ) values for C6BAPE- and TPGDA-LCEs under the three different detachment conditions. Error bars represent  $\pm 1$  standard deviation from the mean. (C) Representative uniaxial stress-strain curves for C6BAPE- and TPGDA-LCEs measured under a ramp displacement rate of 10 mm/s, stretching to 20% and relaxing to zero stress at room temperature (25 °C) in the absence of light. Values for strain energy density (U) are provided for each curve. (D/E) Cyclic tack testing for C6BAPE-LCEs switching between thermal and UV light treatment (D) or UV and blue light treatment (E). Numbers 1 through 4 correspond to processing steps as illustrated in (A) and detailed in *section S2.6* in the SI. (F) Practical demonstration using C6BAPE-LCE for room temperature UV-to-blue light photoswitchable adhesion to pick up and release a glass weight (60 g), showing digital screenshots from Movie S4.

Therefore, thermal-UV cycling is an effective strategy for multistep dry transfer applications requiring switchable adhesives. However, the thermal step is both energy and time intensive, which prompted us to examine fully room temperature photoswitchable adhesion.

Using a modified protocol to that described in Figure 6A we examined UV-visible light cycling to elicit room temperature photoswitchable adhesion (**Figure 6E**). An initial thermal pre-treatment step (70 °C) was employed while pressing the LCE in contact with a smooth glass surface to simultaneously erase thermal history in the bulk and provide an LCE with reduced surface roughness to increase the initial contact area with the quartz plate. This processing step was necessary to maximize  $\sigma_{ad}$  because C6BAPE-LCEs as prepared had a rough surface at room temperature (Figure S14), which likely arose from the above room temperature casting that results in a textured surface upon cooling, common for LCEs. 25,28 Room temperature photorheology was then conducted for C6BAPE-LCEs with a smoothed surface by starting at step (2) of the previous protocol where samples were irradiated with UV light (365 nm, 50 mW/cm<sup>2</sup>) and pressed into the quartz plate with 1 N of force for 5 minutes. Subsequently, samples were detached at a rate of 0.6 mm/minute (previous step 4) and  $\sigma_{ad}$  was measured. This provided an average  $\sigma_{ad}$  of 31 ± 3 kPa. Subsequently, the same step (2) process was employed (UV irradiation and pressing), followed by irradiation with blue light (470 nm, 50 mW/cm<sup>2</sup>) prior to detachment (step 4). This room temperature (25 °C) UV-to-blue light cycle was done to ensure good conformal contact between the C6BAPE-LCE surface and quartz plate by providing an easily deformable isotropic phase with UV light irradiation, followed by photoisomerization with blue light exposure to transition the LCE into an energy dissipating polydomain nematic mesophase and increase  $\sigma_{ad}$ . As desired, the UV-to-blue light cycle increased  $\sigma_{ad}$  to 59.3 ± 0.3 kPa, providing a  $\Delta \sigma_{ad} \approx 2 \times$ . Furthermore, repeating this room temperature photocycling three times provided reproducible changes in adhesion (Figure 6E). Notably, the lower adhesion relative to thermally cycled samples was hypothesized to arise from a reduction in conformal contact. Alternatively, the light-induced mesophase change is likely restricted to the surface due to limited light penetration depth that arises from AZO absorbance, while thermal treatment results in a bulk mesophase change that may increase energy dissipation and  $\sigma_{ad}$  as a result. Regardless, a significant and reproducible change in adhesion ( $\Delta \sigma_{ad} \approx 2^{\times}$ ) was achieved at room temperature using C6BAPE-LCEs by simply toggling the wavelength of light exposure without requiring fast detachment rates.

As a final experiment, a practical demonstration of room temperature photoswitchable adhesion was performed by picking up and then releasing an object via UV-to-blue cycling (**Figure 6F** and Movie S4). Using a C6BAPE-LCE with the same dimensions as that used for the tack tests the sample was first adhered to a glass rod using thermal tape. The sample (~70 mg) was thermally pre-treated to create a smooth surface capable of adhering to and picking up a glass weight (~60 g, image (i)). Irradiating the adhesive with UV light (365 nm, 20 mW/cm², 5 minutes, image (ii)) decreased its adhesion such that it could no longer pick up the weight (image (iii)). However, placing the adhesive in contact with the glass weight and irradiating it with UV light through the glass (image (iv)) followed immediately by blue light irradiation (470 nm, 2 mW/cm², 5 minutes, image (v)) without moving the sample by using a dichroic filter to combine the two LEDs resulted in renewed adhesion strong enough to lift the glass weight (image (vi)). This example showcases the real-life applicability of these LCEs as room temperature photoswitchable adhesives.

#### **CONCLUDING REMARKS**

Azobenzene-containing liquid crystal elastomers (LCEs) were systematically designed, prepared, and characterized to enable room temperature photoswitchable adhesion. Governing principles connecting LCE processing parameters and composition to light-driven changes in molecular order and concomitant optical and physical properties were unveiled. Notably, curing LC resins at a temperature with minimal phase separation that resides between the nematic-to-isotropic transition temperature ( $T_{NI}$ ) of the monomer mixture and resultant LCE provided materials with an ideal photoresponse (i.e., clear  $\Delta T_{NI}$ ). Furthermore,

increasing the AZO content led to a small decrease in  $T_{\rm NI}$  without UV light exposure and a large increase in  $\Delta T_{\rm NI}$ , providing LCEs capable of transitioning from a polydomain nematic state to an isotropic state upon UV light (365 nm) exposure at room temperature. Finally, replacing a non-LC monomer (TPGDA) with an LC one (C6BAPE) increased the processing temperature window, stability of the photostationary (isotropic) state, adhesion strength ( $\sigma_{ad}$ ), and difference in adhesion strength ( $\Delta \sigma_{ad}$ ) between polydomain nematic and isotropic LCE (meso)phases. Simply toggling between UV light (365 nm) and blue light (470 nm) exposure in a tack test gave a  $\Delta \sigma_{ad}$  of 2x, despite the slow pull-off rate (0.6 mm/min), while also showing no significant loss in adhesion over the course of a few cycles. The utility of the "smart" plastic to pick up and release a glass weight that was >800× the mass of the adhesive highlighted its potential applicability for dry transfer of materials from one substrate to another, particularly useful for electronics. Fortuitously, both the materials and processing parameters are modular, and as such we envision that the rate and extent of photoswitchable adhesion can be further optimized. For example, we anticipate that using a higher dose of UV light exposure and/or longer dwell times of pressing could increase  $\sigma_{ad}$  and  $\Delta \sigma_{ad}$ . Additionally, combinations of C6BAPE and TPGDA, or other non-LC acrylics, may lead to LCEs with an attractive combination of softness at room temperature and high energy damping capacity for improved surface contact and  $\sigma_{ad}$ , respectively. Going forward, the inherent spatiotemporal control of light is being examined to create patterned adhesives with directionally dependent (anisotropic) performance. Overall, the revealed design principles will inform the preparation of next generation smart adhesives.

#### ASSOCIATED CONTENT

**Supporting Information**. The supporting information is available free-of-charge via the Internet at http://pubs.acs.org. Additional experimental (materials, instrumentation, and synthesis) and characterization details.

## **AUTHOR INFORMATION**

## **Corresponding Author**

**Zachariah A. Page** – Department of Chemistry, The University of Texas at Austin, Austin, Texas 78712, USA.

Email: zpage@utexas.edu

**Kenneth M. Liechti** – Department of Aerospace Engineering and Engineering Mechanics, The University of Texas at Austin, Austin, TX 78712, USA.

Email: kml@mail.utexas.edu

#### **Author Contributions**

Conceptualization (YW, KML, ZAP); Methodology (YW, BDC, KML, ZAP); Investigation (YW, BDC); Visualization (YW, BDC, ZAP); Funding acquisition (KML, ZAP); Project administration (KML, ZAP); Supervision (KML, ZAP); Writing – original draft (YW, BDC, ZAP); Writing – review & editing (YW, BDC, KML, ZAP).

# **Competing Interests**

None

#### **ACKNOWLEDGMENTS**

The authors acknowledge primary support by the National Science Foundation under Grant No. CMMI-2110526 (YW, BDC, KML, ZAP). Partial support was provided by the Robert A. Welch Foundation under Grant No. F-2007 (ZAP) and the Camille & Henry Dreyfus Foundation under Grant No. TC-23-059 (ZAP).

# References

- (1) Zhang, Y.; Wang, Z.; Yang, Y.; Chen, Q.; Qian, X.; Wu, Y.; Liang, H.; Xu, Y.; Wei, Y.; Ji, Y. Seamless Multimaterial 3D Liquid-Crystalline Elastomer Actuators for next-Generation Entirely Soft Robots. *Sci Adv* **2024**, *6* (9), eaay8606. https://doi.org/10.1126/sciadv.aay8606.
- (2) Rus, D.; Tolley, M. T. Design, Fabrication and Control of Soft Robots. *Nature* **2015**, *521* (7553), 467–475. https://doi.org/10.1038/nature14543.
- (3) El-Atab, N.; Mishra, R. B.; Al-Modaf, F.; Joharji, L.; Alsharif, A. A.; Alamoudi, H.; Diaz, M.; Qaiser, N.; Hussain, M. M. Soft Actuators for Soft Robotic Applications: A Review. *Advanced Intelligent Systems* **2020**, *2* (10), 2000128. https://doi.org/https://doi.org/10.1002/aisy.202000128.
- (4) Amjadi, M.; Turan, M.; Clementson, C. P.; Sitti, M. Parallel Microcracks-Based Ultrasensitive and Highly Stretchable Strain Sensors. *ACS Appl Mater Interfaces* **2016**, 8 (8), 5618–5626. https://doi.org/10.1021/acsami.5b12588.
- (5) Fusco, S.; Huang, H.-W.; Peyer, K. E.; Peters, C.; Häberli, M.; Ulbers, A.; Spyrogianni, A.; Pellicer, E.; Sort, J.; Pratsinis, S. E.; Nelson, B. J.; Sakar, M. S.; Pané, S. Shape-Switching Microrobots for Medical Applications: The Influence of Shape in Drug Delivery and Locomotion. ACS Appl Mater Interfaces 2015, 7 (12), 6803–6811. https://doi.org/10.1021/acsami.5b00181.
- (6) Westbrook, K. K.; Qi, H. J. Actuator Designs Using Environmentally Responsive Hydrogels. *J Intell Mater Syst Struct* **2007**, *19* (5), 597–607. https://doi.org/10.1177/1045389X07077856.
- (7) Heinzmann, C.; Coulibaly, S.; Roulin, A.; Fiore, G. L.; Weder, C. Light-Induced Bonding and Debonding with Supramolecular Adhesives. *ACS Appl Mater Interfaces* **2014**, *6* (7), 4713–4719. https://doi.org/10.1021/am405302z.
- (8) Ferahian, A.-C.; Hohl, D. K.; Weder, C.; Montero de Espinosa, L. Bonding and Debonding on Demand with Temperature and Light Responsive Supramolecular Polymers. *Macromol Mater Eng* **2019**, *304* (9), 1900161. https://doi.org/https://doi.org/10.1002/mame.201900161.
- (9) Bovone, G.; Dudaryeva, O. Y.; Marco-Dufort, B.; Tibbitt, M. W. Engineering Hydrogel Adhesion for Biomedical Applications via Chemical Design of the Junction. *ACS Biomater Sci Eng* **2021**, 7 (9), 4048–4076. https://doi.org/10.1021/acsbiomaterials.0c01677.
- (10) Ribas-Massonis, A.; Cicujano, M.; Duran, J.; Besalú, E.; Poater, A. Free-Radical Photopolymerization for Curing Products for Refinish Coatings Market. *Polymers* **2022**, *14* (14), 2856. https://doi.org/10.3390/polym14142856.
- (11) Kamperman, M.; Synytska, A. Switchable Adhesion by Chemical Functionality and Topography. *J. Mater. Chem.* **2012**, 22 (37), 19390–19401. https://doi.org/10.1039/C2JM31747H.

- (12) Bandara, D.; Burdette, S. Photoisomerization in Different Classes of Azobenzene. *Chem Soc Rev* **2012**, *41*, 1809–1825. https://doi.org/10.1039/c1cs15179g.
- (13) Shibaev, V.; Bobrovsky, A.; Boiko, N. Photoactive Liquid Crystalline Polymer Systems with Light-Controllable Structure and Optical Properties. *Prog Polym Sci* **2003**, 28 (5), 729–836. https://doi.org/https://doi.org/10.1016/S0079-6700(02)00086-2.
- (14) Pang, X.; Lv, J.; Zhu, C.; Qin, L.; Yu, Y. Photodeformable Azobenzene-Containing Liquid Crystal Polymers and Soft Actuators. *Advanced Materials* **2019**, *31* (52), 1904224. https://doi.org/https://doi.org/10.1002/adma.201904224.
- (15) Ito, S.; Yamashita, A.; Akiyama, H.; Kihara, H.; Yoshida, M. Azobenzene-Based (Meth)Acrylates: Controlled Radical Polymerization, Photoresponsive Solid–Liquid Phase Transition Behavior, and Application to Reworkable Adhesives. *Macromolecules* **2018**, *51* (9), 3243–3253. https://doi.org/10.1021/acs.macromol.8b00156.
- (16) Zhou, H.; Xue, C.; Weis, P.; Suzuki, Y.; Huang, S.; Koynov, K.; Auernhammer, G. K.; Berger, R.; Butt, H.-J.; Wu, S. Photoswitching of Glass Transition Temperatures of Azobenzene-Containing Polymers Induces Reversible Solid-to-Liquid Transitions. *Nat Chem* 2017, 9 (2), 145–151. https://doi.org/10.1038/nchem.2625.
- (17) Xu, G.; Li, S.; Liu, C.; Wu, S. Photoswitchable Adhesives Using Azobenzene-Containing Materials. *Chem Asian J* **2020**, *15* (5), 547–554. https://doi.org/https://doi.org/10.1002/asia.201901655.
- (18) Kim, D.; Kim, H.; Jeon, W.; Kim, H.-J.; Choi, J.; Kim, Y.; Kwon, M. S. Ultraviolet Light Debondable Optically Clear Adhesives for Flexible Displays through Efficient Visible-Light Curing. *Advanced Materials* **2023**, *36* (14), 2309891. https://doi.org/https://doi.org/10.1002/adma.202309891.
- (19) Ohzono, T.; Saed, M.; Terentjev, E. Enhanced Dynamic Adhesion in Nematic Liquid Crystal Elastomers. *Advanced Materials* **2019**, *31* (30), 1902642. https://doi.org/10.1002/adma.201902642.
- (20) Benedek, I.; Feldstein, M. M. Fundamentals of Pressure Sensitivity; CRC Press, 2008. https://doi.org/10.1201/9781420059380.
- (21) Creton, C.; Ciccotti, M. Fracture and Adhesion of Soft Materials: A Review. *Rep Prog Phys* **2016**, 79, 046601. https://doi.org/10.1088/0034-4885/79/4/046601.
- (22) Saed, M. O.; Gablier, A.; Terentjev, E. M. Exchangeable Liquid Crystalline Elastomers and Their Applications. *Chemical Reviews* **2022**, *122* (5), 4927–4945. https://doi.org/10.1021/acs.chemrev.0c01057.
- (23) Creton, C. Pressure-Sensitive Adhesives: An Introductory Course. *MRS Bull* **2003**, 28 (6), 434–439. https://doi.org/10.1557/mrs2003.124.
- (24) Pranda, P. A.; Hedegaard, A.; Kim, H.; Clapper, J.; Nelson, E.; Hines, L.; Hayward, R. C.; White, T. J. Directional Adhesion of Monodomain Liquid Crystalline Elastomers. *ACS Appl Mater Interfaces* **2024**, *16* (5), 6394–6402. https://doi.org/10.1021/acsami.3c16760.

- Ohzono, T.; Koyama, E. Enhanced Photocontrollable Dynamic Adhesion of Nematic Elastomers on Rough Surfaces. *Polymer* **2022**, 260, 125377. https://doi.org/https://doi.org/10.1016/j.polymer.2022.125377.
- (26) Ohzono, T.; Minamikawa, H.; Koyama, E.; Norikane, Y. Unlocking Entropic Elasticity of Nematic Elastomers Through Light and Dynamic Adhesion. *Adv Mater Interfaces* **2021**, 8 (14), 2100672. https://doi.org/https://doi.org/10.1002/admi.202100672.
- (27) Annapooranan, R.; Suresh Jeyakumar, S.; J. Chambers, R.; Long, R.; Cai, S. Ultra Rate-Dependent Pressure Sensitive Adhesives Enabled by Soft Elasticity of Liquid Crystal Elastomers. *Adv Funct Mater* **2024**, *34* (1), 2309123. https://doi.org/https://doi.org/10.1002/adfm.202309123.
- Ware, T. H.; Biggins, J. S.; Shick, A. F.; Warner, M.; White, T. J. Localized Soft Elasticity in Liquid Crystal Elastomers. *Nat Commun* **2016**, *7* (1), 10781. https://doi.org/10.1038/ncomms10781.
- (29) E M Terentjev. Liquid-Crystalline Elastomers. *Journal of Physics: Condensed Matter* **1999**, *11* (24), R239. https://doi.org/10.1088/0953-8984/11/24/201.
- (30) Mistry, D.; Traugutt, N. A.; Sanborn, B.; Volpe, R. H.; Chatham, L. S.; Zhou, R.; Song, B.; Yu, K.; Long, K. N.; Yakacki, C. M. Soft Elasticity Optimises Dissipation in 3D-Printed Liquid Crystal Elastomers. *Nat Commun* **2021**, *12* (1), 6677. https://doi.org/10.1038/s41467-021-27013-0.
- Guo, H.; Saed, M. O.; Terentjev, E. M. Mechanism of Pressure-Sensitive Adhesion in Nematic Elastomers. *Macromolecules* **2023**, 56 (16), 6247–6255. https://doi.org/10.1021/acs.macromol.3c01038.
- (32) Gao, Y.; Wu, K.; Suo, Z. Photodetachable Adhesion. *Advanced Materials* **2019**, *31* (6), 1806948. https://doi.org/10.1002/adma.201806948.
- (33) Saed, M. O.; Torbati, A. H.; Starr, C. A.; Visvanathan, R.; Clark, N. A.; Yakacki, C. M. Thiol-Acrylate Main-Chain Liquid-Crystalline Elastomers with Tunable Thermomechanical Properties and Actuation Strain. *J Polym Sci B Polym Phys* **2017**, *55* (2), 157–168. https://doi.org/https://doi.org/10.1002/polb.24249.
- (34) Barnes, M.; Cetinkaya, S.; Ajnsztajn, A.; Verduzco, R. Understanding the Effect of Liquid Crystal Content on the Phase Behavior and Mechanical Properties of Liquid Crystal Elastomers. *Soft Matter* **2022**, *18*, 5074-5081. https://doi.org/10.1039/D2SM00480A.
- (35) Hebner, T.; Bowman, C.; White, T. The Contribution of Intermolecular Forces to Phototropic Actuation of Liquid Crystalline Elastomers. *Polym Chem* **2021**, *12*, 1581-1587. https://doi.org/10.1039/D1PY00028D.
- (36) Bauman, G. E.; McCracken, J. M.; White, T. J. Actuation of Liquid Crystalline Elastomers at or Below Ambient Temperature. *Angewandte Chemie International Edition* **2022**, *61* (28), e202202577. https://doi.org/https://doi.org/10.1002/anie.202202577.
- (37) Liu, X. F.; Luo, X.; Liu, B. W.; Zhong, H. Y.; Guo, D. M.; Yang, R.; Chen, L.; Wang, Y. Z. Toughening Epoxy Resin Using a Liquid Crystalline Elastomer for Versatile Application. *ACS Appl Polym Mater* **2019**, *1* (9), 2291–2301. https://doi.org/10.1021/acsapm.9b00319.

- (38) Mistry, D.; Nikkhou, M.; Raistrick, T.; Hussain, M.; Jull, E. I. L.; Baker, D. L.; Gleeson, H. F. Isotropic Liquid Crystal Elastomers as Exceptional Photoelastic Strain Sensors. *Macromolecules* **2020**, *53* (10), 3709–3718. https://doi.org/10.1021/acs.macromol.9b02456.
- (39) Wolff, L. B.; Mancini, T. A.; Pouliquen, P.; Andreou, A. G. Liquid Crystal Polarization Camera. *IEEE Transactions on Robotics and Automation* **1997**, *13* (2), 195–203. https://doi.org/10.1109/70.563642.
- (40) Haller, I. Thermodynamic and Static Properties of Liquid Crystals. *Progress in Solid State Chemistry* **1975**, *10*, 103–118. https://doi.org/10.1016/0079-6786(75)90008-4.
- (41) Yusuf, Y.; Sumisaki, Y.; Kai, S. Birefringence Measurement of Liquid Single Crystal Elastomer Swollen with Low Molecular Weight Liquid Crystal. *Chem Phys Lett* **2003**, *382*, 198–202. https://doi.org/10.1016/j.cplett.2003.09.089.
- (42) Kumar, A. Calculation of Optical Parameters of Liquid Crystals. *Acta Phys Pol A* **2007**, *112*, 1213–1221. https://doi.org/10.12693/APhysPolA.112.1213.